

Article

Design, Multi-Objective Optimization, and Prototyping of a 20 kW 8000 rpm Permanent Magnet Synchronous Motor for a Competition Electric Vehicle

Pedro P. C. Bhagubai ¹, João G. Sarrico ², João F. P. Fernandes ^{1,*} and P. J. Costa Branco ¹

¹ IDMEC, Instituto Superior Técnico, Universidade de Lisboa, 1049-001 Lisbon, Portugal; pedro.bhagubai@tecnico.ulisboa.pt (P.P.C.B.); pbranco@tecnico.ulisboa.pt (P.J.C.B.)

² Instituto Superior Técnico, Universidade de Lisboa, 1049-001 Lisbon, Portugal; viseu.sarrico@tecnico.ulisboa.pt

* Correspondence: joao.f.p.fernandes@tecnico.ulisboa.pt

Received: 6 April 2020; Accepted: 12 May 2020; Published: 14 May 2020



Abstract: A high-performance 20 kW, 20 Nm, 8000 rpm, spoke-type interior permanent magnet motor to be integrated into a FormulaStudent electric car's powertrain has been designed to meet demanding performance requirements for its driving cycle. This paper describes key steps in the design optimization, analysis, fabrication, and testing of this machine. Design optimization used the non-dominated sorting genetic algorithm II (NSGA-II) coupled with a hybrid analytical/finite element model to reduce the computational time, achieving a torque and efficiency of 20 Nm and 98.6%, respectively. A prototype has been constructed. The final motor design has been tested, where experimental nominal torque and efficiency have reached 18.2 Nm and 90%, respectively. Design challenges regarding the manufacturing are presented, justified, and discussed in detail. Test results were conducted to evaluate reliability and motor temperatures with and without water refrigeration at nominal current. Despite those adjustments in the optimized design, one shows that the impact on the car's lap time was low, going from 77.3 s for the ideal optimized motor to 78.9 s for the prototyped motor.

Keywords: electromagnetic modeling; multi-objective optimization; permanent magnet; synchronous motor

1. Introduction

This work contributes to the research and development of high-performance electric vehicles by designing, optimizing, and prototyping a 20kW 8000 rpm permanent magnet synchronous motor for the electric vehicle of FormulaStudent (FST) competitions, considering a typical driving cycle. Due to the multiple numbers of physics, variables, and constraints and the non-linearity of materials, the optimization of the motor was done using a genetic algorithm based on a hybrid analytical/finite element model.

In recent years, electric cars have entered the motorsport environment, with the adoption of hybrid systems in Formula 1 and the creation of formula E exclusively for electric race cars. These competitions provide an opportunity to test and validate state-of-the-art technologies and to analyze the possibility of integrating them into passenger's road cars. Formula Student is an international engineering competition where teams of students design, build, and race electric vehicles. The competition provides an opportunity to design and manufacture all parts of an electric competition car, including the motor, an essential component of a car's powertrain. Designing a custom motor allows building an entire car under FST rules and the team's requirements and specifications, instead of adopting a commercially available solution and building a car around it. Most FST racing tracks are meandering circuits with

many curves and short straights. This favors cars that corner fast and recover speed quickly. Because acceleration is more relevant than top speed in competition, four wheel drive electric cars are typically desired, with optimized motors to develop the highest torque with the lowest weight.

The choice of motor topology has a significant impact on the car's performance. Several studies focused on the comparison between the possible specific-power and efficiency range for different types of electrical machines, consistently identifying the PMSM (permanent magnet synchronous machines) as the ones with higher values [1–3]. The downsides are increased cost because of the permanent magnets (PM) and the risk of demagnetization from cracks caused by vibrations or high temperatures during motor operation, causing a loss of power [4]. These PMs can be surface or interior mounted. Interior permanent magnet synchronous machines (IPSM) present, in general, higher mechanical reliability, reduced demagnetization risk, and smaller airgap, when compared to the surface, mounted permanent magnet machines [5]. In an IPSM, the magnets can be arranged in a radial or spoke type topology in the rotor. The advantage of the spoke-type IPSM machines is the higher concentration of magnetic flux in the airgap that results in higher torque density [6]. Therefore, there is a more efficient use of the PM materials in the spoke type IPSM machines. Its main disadvantages being the leakage flux in the rotor, closer to the shaft [5], and high torque-ripple due to the high flux concentration in the air-gap [7]. A spoke-type IPSM topology is chosen for the powertrain of the FST electric car because its high torque density characteristic aligns with the high acceleration requirement in FS racing tracks.

Regarding the electrical machine's optimization, several multi-objective optimization tools have been applied to electrical machines. Several types of optimization methods have been studied. In [8], the design of a PMSM was optimized using a global-simplex optimization algorithm, using a finite element analysis (FEA) method as a base model. In [9], the shape of the rotor magnetic core was optimized using a map of sections that can be of air or magnetic material, using a hybrid algorithm, based on a genetic algorithm and FEA model. In [10], a non-dominated sorting genetic algorithm II (NSGA-II) algorithm was used to design a vanadium-cobalt-iron (VaCoFe) core of a single-phase machine, showing an increase of specific power in 20% when compared with silicon-iron (FeSi) at 50 Hz applications. In [11], a new preliminary approach of optimizing characteristics of the electrical machine to maximize its performance under a typical driving cycle was performed. This latter approach is critical in the optimization of electrical machines for high-performance electrical vehicles, where energy efficiency and specific power is critical. Therefore, the use of optimization tools based on hybrid analytical/finite-element models is a successful method, in particular to spoke-type internal permanent magnet synchronous machines (IPMSMs) [7–9,12]. These provide sufficient accuracy with lower computation times than using only finite-element models [13].

Within this context, this work proposes the design, optimization, and prototyping of a 20 kW permanent magnet synchronous motor for the electric vehicle of FormulaStudent competitions, considering a typical driving cycle. Due to the multiple number of physics, variables, and constraints and the non-linearity of materials, the optimization of the motor was done using the genetic algorithm non-dominated sorting genetic algorithm II (NSGA-II) based on a hybrid analytical/finite-element model. This hybrid model presents sufficient accurate electromagnetic and thermal results and, at the same time, can be computed within a feasible time for the optimization process. The model is composed of a stationary time 2D finite element model, to calculate the motor's main parameters, as d - q inductances, permanent magnet flux distribution, losses, and an auxiliary script to compute analytically the voltage, torque, and efficiency curves. Using results from optimization, a prototype was developed and tested in a laboratorial environment. The nominal torque and power, and the nominal and maximum speeds of the developed prototype are 18.2 Nm, 17.2 kW, and 8000 rpm and 12,000 rpm, respectively.

2. Specification Requirements

Due to the specific motorsport application, the power and torque requirements were estimated using a detailed analysis tool for racing tracks: OptimumLap software (version 1.5.5, OptimumG,

Centennial, CO, USA) [14]. With parameters, such as expected vehicle mass, tires, suspension, maximum power, and track geometry, it is possible to estimate the required torque and power along the track for the best possible lap-time. The maximum power of the electric car is limited to 80 kW by FormulaStudent competition rules.

The electric motor is to be optimized considering the track geometry of the FSAE autocross Germany track in Figure 1. It presents a high number of turns, and the maximum race duration is 30 min, as imposed by the FormulaStudent competition. In Figures 1 and 2 the optimized power and torque required by the motor are shown, respectively, that maximizes the number of laps made in 30 min. Due to a large number of curves, power reduces during the curves and is consequently increased after each one, leading to peaks around 80 kW (with torque values of 80 Nm).

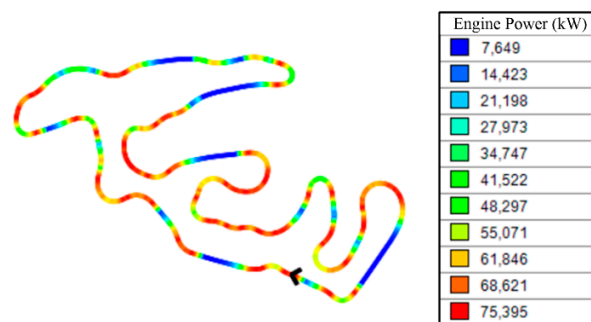


Figure 1. FSAE autocross Germany track simulation.

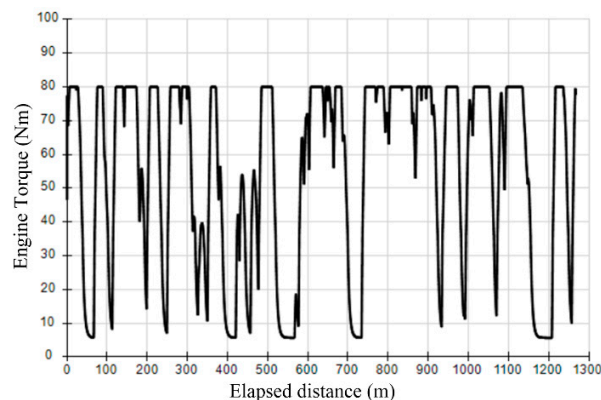


Figure 2. Instantaneous motor's torque along the track.

Because most FormulaStudent racing tracks are meandering circuits with many curves and short straights, high acceleration is the most critical parameter. From the point of view of the powertrain, low weight and high traction and torque are desirable. The chosen topology for the FormulaStudent car is that of four electric motors with fixed gear transmission, each one mounted in the suspension system of each wheel. One inverter is connected per motor. These are all controlled individually by a central torque vectoring controller and connected to the same battery pack. This solution allows the increased traction of a four-wheel-drive system, and because it does not require a mechanical differential or a weighty transmission, it is a light and less complex system [15].

The FormulaStudent car is redesigned every year by the developing team to keep a constant search for higher performances. Therefore, some components are reused in the following year, and, in this case, the transmission and electronic inverters were already defined. The existent transmission gear has a fixed ratio of 1:5, and the inverters have a rated voltage, current, and frequency of 380 V, 100 A, and 400 Hz, respectively, and equipped with a field-oriented control (FOC) method. This determines maximum rotation speed, voltage, and electrical current requirements.

The motors are chosen to be spoke-type internal permanent magnet synchronous machines (IPMSM) because of their typical higher efficiency, responsivity, torque, and power densities [4–7]. The set requirements, for each motor to be installed at each wheel, are presented in Table 1. The maximum power and torque values (80 kW and 80 Nm) are distributed uniformly between each motor. Therefore, each motor’s rated power and torque will be 20 kW and 20 Nm, respectively. The maximum voltage and peak current are imposed by the inverters.

Table 1. Requirements for each internal permanent magnet synchronous machine (IPMSM).

Requirement	Value
Nominal power	20 kW
Maximum torque	20 Nm
Rated speed	8000 rpm
Maximum speed	12,000 rpm
Maximum voltage *	380 V
Peak current *	100 A

* set by the inverters.

3. Electric Motor Materials

The materials chosen for the IPMSM will determine the motor’s performance. The soft magnetic material that constitutes the machine’s stator and rotor will impose a magnetic saturation point. The Joule losses from the magnetic core and windings will impact the operating temperature. The mechanical properties of the shaft and rotor will limit the achievable maximum rotational speed without material failure.

On the other hand, the cost and availability of the material is also an important aspect to be considered due to budget limitations. Therefore, the choice of materials is subject to a tradeoff between their properties and their cost. These were chosen to give the best results for a reasonable price.

3.1. Magnetic Core

The magnetic core of the IPMSM, both rotor and stator, is made of soft magnetic material. Desirable properties are high permeability and saturation point, low losses, and, for the rotor, sufficient mechanical strength to support the required rotational speed [16]. In this application, as the electric frequency will reach values around 400 Hz, the magnetic core losses will have a high impact on the IPMSM performance (losses increase with frequency). It was chosen a silicon-iron (FeSi) alloy, instead of a vanadium-cobalt-iron (VaCoFe) one, due to the impact of the VaCoFe’s core losses at high electric frequencies. Research [10] presented a comparison between a FeSi and a VaCoFe magnetic core, regarding their efficiency and specific power. While the VaCoFe allows the increase of around 17% of specific power, with similar levels of efficiency, for an electric frequency of 50 Hz, it shows some limitations for 400 Hz due to its core losses. Therefore, the chosen magnetic material core was NGO 35JN200 non-oriented electrical steel, in Table 2 [17], that offers a saturation point of around 1.7–1.8T, presents low core losses, and has adequate tensile strength. Its B-H curve and core density losses are shown in Figures 3 and 4, respectively, for the electrical frequency of 400 Hz curves.

Table 2. Mechanical properties of NGO 35JN200 electrical steel.

Property	NGO 35JN200
Ultimate Tensile Strength	450 MPa
Density	7.65 g/cm ³

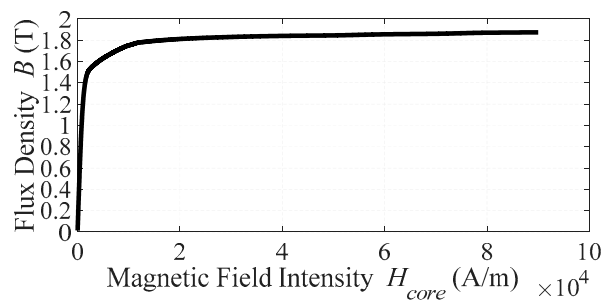


Figure 3. B-H curve of NGO 35JN200 electrical steel.

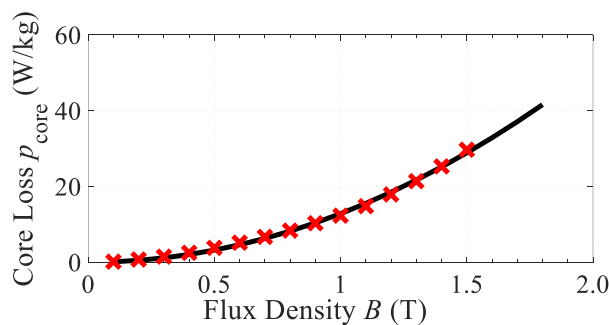


Figure 4. Core loss curve at 400 Hz of NGO 35JN200 electrical steel.

3.2. Shaft

The shaft must be designed to withstand the centrifugal forces at maximum speed (12,000 rpm) and also a safety margin to accommodate a faulty operation of 15,000 rpm, and the generated torque, so that it is transmitted to the wheels correctly. Due to the typical magnetic leakage present in spoke-type IPMSM [5], the rotor shaft must be made from a non-ferromagnetic material. Besides, low electric conductivity is desired, so that induced currents are reduced [18]. Thus, the desired properties are high tensile strength, low electrical conductivity, and low magnetic permeability. The material chosen is stainless steel ASI 316, with the characteristics presented in Table 3 [19]. Special attention must be given to the yield tensile strength of 290 MPa, which is higher than the one obtained from during the mechanical simulations (206.8 MPa, as will be shown in the results section).

Table 3. Properties of stainless steel ASI 316.

Property	Stainless Steel ASI 316
Density	8.00 g/cm ³
Yield tensile strength	290 MPa
Electrical resistivity	75 $\mu\Omega$.cm
Thermal conductivity	16.2 W/(m.K)
Magnetic relative permeability	1.0008

3.3. Permanent Magnets

In the IPMSM, permanent magnets provide the field excitation. The main properties to be considered when choosing permanent magnet materials are high energy density, magnetic coercivity, remnant magnetic flux density, and working temperature. Neodymium-iron-boron (NdFeB) is the most preferred material in electrical machine design due to its higher values of energy density and remnant magnetic flux density than other alternatives [4], with reasonable operating temperature. Their main characteristics are listed in Table 4. The N40H grade NdFeB magnet was chosen as it presented reasonable maximum operating temperature and high energy density at a moderate cost.

Its main characteristics are listed in Table 4 [20]. For simulation and optimization, the permanent magnet's remnant magnetic flux was taken from the material's demagnetization curve at a maximum operating temperature, 120 °C, as $B_r = 1.2$ T to account for its reduction with temperature.

Table 4. Properties of N40H grade neodymium-iron-boron (NdFeB) permanent magnet material.

Property	NdFeB N40H
Residual magnetic flux density	1.36 ± 0.03 T at 20 °C
Coercivity	1051 ± 56 kA/m
Energy product	357 ± 16 kJ/m ³
Max. operating temperature	120 °C
Curie temperature	320 °C

4. Spoke-Type Interior Permanent Magnet Synchronous Machines (IPSM) Model

The chosen motor topology is that of a spoke-type interior permanent magnet synchronous motor (IPMSM) because of its typical high efficiency and power/torque density [4]. The interior radially magnetized permanent magnets allow higher mechanical reliability, reduced demagnetization risk, and smaller airgap than surface-mounted magnets [5], together with a flux-concentrating topology that results in higher torque density [6].

4.1. Geometry

Figure 5 presents the geometry of the IPMSM to be optimized. The dimension parameters will be decision variables that define specific designs during optimization. These are the rotor, r_r , and shaft radius, r_s , the permanent magnet width, w_m , and length, l_m , the stator tooth width, w_t , length, l_t , and outer ring width, w_s , and the airgap size, g . The outer radius and length of the motor are dependent on the space available near each wheel, and its maximum values are equal to 50 mm and 80 mm, respectively.

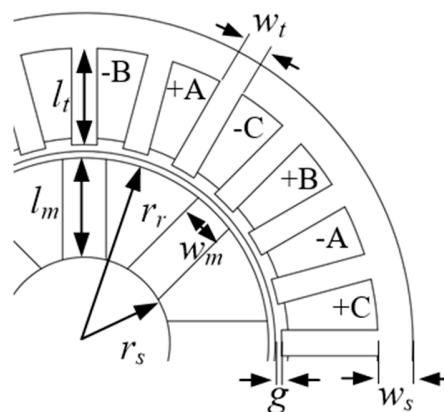


Figure 5. Interior permanent magnet synchronous machines (IPSM) model geometry with 24 slots.

4.2. Winding Layout Analysis

The airgap magnetomotive force (mmf) wave will influence the mean and ripple torque values and is highly dependent on the winding arrangement and airgap length. The spatial mmf harmonics are produced by the discretization of the stator slots. These harmonics cause torque ripple, vibration, and reduced efficiency.

To find the best winding layout, the method presented in [21], based on a multi-objective optimization algorithm, was used. The airgap mmf harmonic analysis is based on the distribution of the conductors around the stator periphery. Assuming that the conductors are located at the slot opening, winding conductor distribution for each w -th winding, $\overline{C_w^v}$, with m coils in series is obtained

from (1) and its resulting airgap *mmf*, F_w , is given by (2). In these, N_n is the number of turns in a coil, d is the mean airgap diameter, K_p^v is the v -th harmonic pitch factor, k the harmonic wave number, x_n the n -th coil axis position and i_w the w -th winding current. The total airgap *mmf* is obtained from summing the contributions from each phase winding.

$$\overline{C}_w^v = -\frac{2jN_n}{\pi d} \sum_{n=1}^m K_p^v e^{jkx_n} \quad (1)$$

$$F_w(x, t) = i_w(t) \sum_{v=-\infty}^{\infty} \left(\frac{j}{k}\right) \overline{C}_w^v e^{-jkx} \quad (2)$$

For single or double-layer winding and a given number of slots, poles, and phases, the algorithm searches the space of possible winding layouts, optimizing for multiple objective functions: maximize the fundamental component of the *mmf* per ampere in the airgap given by $\left| \sum_{w=1}^{N_{phases}} \frac{F_w^{v=n_{pp}}(x, t)}{i_w(t)} \right|$, with n_{pp} the number of pole pairs; and minimize the sum of its harmonics, $\left| \sum_{w=1}^{N_{phases}} \frac{F_w^{v \neq n_{pp}}(x, t)}{i_w(t)} \right|$, while maintaining a balanced winding condition.

The required number of poles that meet the velocity requirement for the inverter frequency is 8, 10, or 12 poles. Combinations of these number of poles with 12, 24, and 30 stator slots were considered for optimization. A single layer coil structure was selected to simplify the future manufacturing process. Table 5 presents the optimized results for each number of slots/poles combination, resulting airgap *mmf*/ampere harmonic analysis, and whether the balanced winding condition is fulfilled or not. The adopted solution is 24 stator slots with 8 rotor poles, with the configuration presented in Figure 5. This solution gives a good compromise between a high fundamental component and low harmonics while satisfying the balanced winding condition.

Table 5. Motor winding layout analysis results.

Study	Airgap <i>mmf</i> /ampere Fundamental Component	Airgap <i>mmf</i> /ampere Sum of Harmonics	Balanced Condition
12 slots/6 poles	0.574	1.790	Yes
12 slots/8 poles	0.414	1.169	Yes
12 slots/10 poles	0.369	2.137	No
24 slots/6 poles	0.979	2.512	Yes
24 slots/8 poles	0.956	0.414	Yes
24 slots/10 poles	0.732	2.394	Yes
30 slots/6 poles	1.501	2.630	No
30 slots/8 poles	0.88	3.576	No
30 slots/10 poles	0.902	2.097	No

4.3. Electromagnetic Model

An analytical and finite element (FE) based model of the IPMSM is used to assure a high model accuracy and relatively low computational time. The computational time is critical for the optimization process as, typically, during optimization, a high number of geometries are simulated.

This model consists of an equivalent circuit based on a synchronous d - q reference frame considering iron losses, Figure 6, where the lumped parameters such as d - q inductances, L_d and L_q , and iron core resistance, R_c , are estimated with results from a stationary-time 2D FE model. The steady-state equations that describe the three-phase machine are given by (3)–(7), where v_d , v_q , i_d , i_q are the d - q axis stator voltages and currents, i_{od} , i_{oq} are the torque generating currents, R_s is the phase winding resistance, R_c is the equivalent core-loss resistance, L_d and L_q are the d - q inductances, ω_M is the rotor angular speed, and Ψ_{PM} the permanent magnet linked flux which, for the considered machine topology,

is aligned with the d -axis. In (3), the generated torque, T , has two components: the electromagnetic one, T_{EM} , and reluctance one, T_{Rel} .

$$v_d = R_s i_d - \omega_M L_q i_{oq} \tag{3}$$

$$v_q = R_s i_q + \omega_M (L_d i_{od} + \Psi_{PM}) \tag{4}$$

$$T = T_{EM} + T_{Rel} = \frac{3}{2} n_{pp} (\Psi_{PM} i_{oq} + (L_d - L_q) i_{od} i_{oq}) \tag{5}$$

$$i_d = i_{od} - \frac{\omega_M L_q i_{oq}}{R_c} \tag{6}$$

$$i_q = i_{oq} + \frac{\omega_M (L_d i_{od} + \Psi_{PM})}{R_c} \tag{7}$$

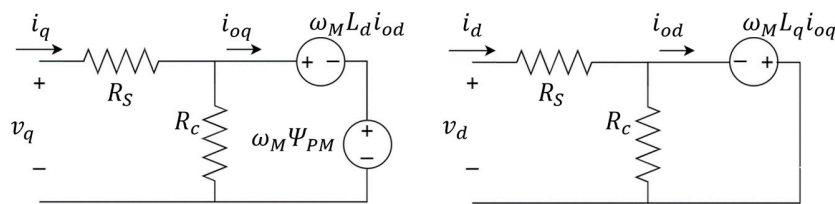


Figure 6. Synchronous machine equivalent circuit considering core-losses in d - q reference frame.

The estimation of iron losses, in this type of model, is usually made by time-dependent simulation for a certain rotation speed to consider flux density harmonics in the core [22]. Because a genetic optimization algorithm is to be applied, the model must be computationally fast. As such, time-dependent analysis is avoided. For optimization purposes, a rough estimation of iron losses is enough, and a more accurate loss model can be applied to the selected optimized motor’s design to refine the obtained solutions. Additionally, because traction application motors work at variable speed, iron losses are estimated for the worst-case by the locked-rotor method [23]. With these considerations, core loss density, p_{core} , is roughly estimated with Steinmetz coefficients, obtained from loss curve data, considering a sinusoidal variation of the flux density in the rotor and stator cores (8). In this, f is the frequency of the flux density, B_m is the amplitude of the flux density, and k_h , k_e and k_{exc} are the hysteresis, eddy current, and excess losses coefficients. The amplitude of flux density is obtained from the stationary FE model, with the stator flux aligned with d and q rotor axes. As a result, the effects of minor loops and DC bias on hysteresis losses on the rotor core are also ignored [24].

$$p_{core} = k_h f B_m^2 + k_e (f B_m)^2 + k_{exc} (f B_m)^{1.5} \tag{8}$$

Losses density in PMs, p_{PM} , are estimated with an analytical model for parallelepiped shape magnets, not considering skin effect (9) [25]. In (9), ρ_{PM} , d_{PM} , and l_{PM} are the resistivity, depth, and length of the permanent magnet, respectively. The effect of permanent magnet eddy currents on the magnetic flux distribution is not considered as the B_m is obtained from magnetostatic stationary time 2D FE simulation. In some systems, this effect can have an impact on output torque in some purely magnetic systems such as magnetic gear [26]. However, it is not as relevant for IPSPMs and optimization purposes. To account for the reduction of the remnant magnetic flux density in the PMs, the operating temperature of 120 °C was considered. The core loss density is then used to compute R_c given by (10), considering core and permanent magnet losses, where V_{core} and V_{PM} are the rotor plus stator core volume and permanent magnets volume, respectively.

$$p_{PM} = \frac{(\pi f B_m)^2}{8 \rho_{PM}} \frac{d_{PM}^2 l_{PM}^2}{d_{PM}^2 + l_{PM}^2} \tag{9}$$

$$R_c = \frac{3}{2} \frac{(\omega_M(L_d i_{od} + \Psi_{PM}))^2 + (\omega_M L_q i_{oq})^2}{p_{core} V_{core} + \rho_{PM} V_{PM}} \quad (10)$$

The L_d and L_q inductances and ψ_{PM} are computed from the results of linked flux obtained from the stationary FE model. Without considering permanent magnets flux ($\Psi_{PM} = 0$), Ψ_d and Ψ_q are obtained as a function of i_{od} and i_{oq} currents, by aligning the rotor d and q axes with the stator in positions of maximum and minimum flux linkage with stator coil (coil A). L_d and L_q are estimated from (11). The permanent magnet linked flux, ψ_{PM} , is obtained by aligning d -axis with stator coil A, with zero current ($i_d = 0$) and measuring the d -axis linked flux. During optimization, for simplification, cross saturation is neglected, and L_d, L_q are estimated as depending only on respective i_{od} and i_{oq} (12).

$$L_d(i_{od}, i_{oq}) = \left. \frac{\Psi_d}{i_{od}} \right|_{\Psi_{PM}=0} \quad (11)$$

$$L_q(i_{od}, i_{oq}) = \left. \frac{\Psi_q}{i_{oq}} \right|_{\Psi_{PM}=0}$$

$$L_d = \left. \frac{\Psi_d}{i_{od}} \right|_{i_{oq}=0} \quad (12)$$

$$L_q = \left. \frac{\Psi_q}{i_{oq}} \right|_{i_{od}=0}$$

4.4. Estimation of Maximum Operating Temperature

The thermal phenomena in the machine are critical to determining if a design is viable or not. As it is required to estimate the maximum operating temperature of the machine during optimization, a simplified model was used to reduce the computational time. For the desired application, the motor will be required to provide maximum torque/power in short repeated bursts, as seen in Figure 2. The instantaneous temperature will be lower or equal to the steady-state temperature during the desired working time. Therefore, we can estimate the maximum operating temperature for the worst-case scenario and evaluate if the optimized solutions are viable.

The machine will be water-cooled by a previously designed system that achieves a heat transfer coefficient of $h = 500 \text{ W m}^{-2} \text{ K}^{-1}$ [27]. For liquid-cooled forced convection, typical heat transfer coefficient values are between 50 to 20,000 $\text{Wm}^{-2} \text{ K}^{-1}$ [28].

The estimation model considers the heat dissipation from the machine surface to the cooling system and environment and convective heat transfer in the airgap. Thermal conduction in the rotor and stator core is neglected as the conductive thermal resistance in metallic materials is very low compared to the convective resistance of the airgap, the latter being a limiting factor on the operating temperature of the rotor and permanent magnets. The machine produces heat from Joule losses in the rotor core, (8), and PMs (9), which is dissipated through the airgap and, together with stator core and copper windings' losses (13), through the cooling jacket and into the environment. The considered thermal circuit is presented in Figure 7. This simplified model roughly estimates steady-state temperatures and is used only to evaluate whether the thermal constraint during optimization is violated.

$$P_{Cu} = \frac{3}{2} R_s (i_d^2 + i_q^2) \quad (13)$$

The airgap convective heat transfer coefficient (14) is obtained from dimensionless correlations obtained for heat transfer in flow between concentric rotating cylinders (15) [29]. These correlations depend on a Taylor number, Ta (16), that indicates whether the flow in the airgap is laminar or turbulent. In (14)–(16), k is the air's thermal conductivity, $D_h = \frac{2(\pi((r_r+g)^2-r_r^2))}{\pi((r_r+g)-r_r)}$ is the hydraulic diameter, Nu the Nusselt number, ν the air's kinematic viscosity, and ω the rotor's mechanical rotational speed. For the

typical range of this motor’s speed and the considered geometrical dimensions, $Ta > 10^4$, and the flow will be turbulent with Nu is given by (15).

$$h_{ag} = \frac{k}{D_h} Nu \tag{14}$$

$$Nu = 0.409 Ta^{0.241} \tag{15}$$

$$Ta = \frac{\omega^2 (r_r + g) \left(\frac{D_h}{2}\right)^3}{\nu^2} \tag{16}$$

The heat transfer coefficients are used to compute the thermal resistances of the airgap (17) and the machine’s surface to the environment through the cooling system (18), as in the thermal circuit in Figure 7. In (18) and (19), $S_{ag} = 2\pi r_r L$ is the heat transfer surface of the airgap and $S = 2\pi RL$ is the electric machine’s surface area with outer radius R and length L . The heat transfer is described by the thermal equation system (19), where T_s and T_{amb} are the surface and ambient temperatures.

$$R_{ag} = \frac{1}{h_{ag} S_{ag}} \tag{17}$$

$$R_S = \frac{1}{hS} \tag{18}$$

$$\begin{cases} T_s = R_S(P_{stator} + P_{Cu}) + T_{amb} \\ T_{rotor} = R_{ag}(P_{rotor} + P_{PM}) + T_s \end{cases} \tag{19}$$

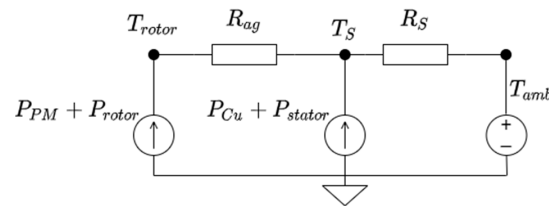


Figure 7. Thermal circuit used to estimate the maximum operating temperature during optimization.

4.5. Finite Element Model

A 2D finite element (FE) model is used, not only to estimate the d - q inductances, L_d and L_q , and iron core resistance, R_c , but also to verify if any part of the magnetic core is reaching saturation. Because multi-objective optimization is performed with a genetic algorithm, the FE model must be computationally fast and sufficiently accurate. As such, only one pole of the machine is simulated, cut along flux density distribution symmetry lines with continuity conditions imposed on the boundaries, Figure 8. Each domain is defined as the correspondent materials described previously: copper coils, NGO 35JN200 magnetic core, NdFeB PMs, and stainless-steel shaft.

A stationary-time simulation for the d - q axes is considered, and the current in each phase is given by (20). Depending on if the rotor’s q ($\theta = 90^\circ$) or d ($\theta = 0^\circ$) axis is aligned with phase A, the Park transformation results in $i_d = 0$ and $i_q = I_m$ or $i_d = I_m$ and $i_q = 0$, (21), respectively. By adjusting θ , d - q linked fluxes Ψ_q and Ψ_d , and B_q and B_d flux density distributions can be estimated from the model simulation.

$$\begin{aligned} I_A &= I_m \cos(\omega t) \\ I_B &= I_m \cos\left(\omega t - \frac{2\pi}{3}\right) \\ I_C &= I_m \cos\left(\omega t + \frac{2\pi}{3}\right) \end{aligned} \tag{20}$$

$$\begin{bmatrix} i_d \\ i_q \end{bmatrix} = \begin{bmatrix} \cos(\theta) & \cos\left(\theta - \frac{2\pi}{3}\right) & \cos\left(\theta + \frac{2\pi}{3}\right) \\ -\sin(\theta) & -\sin\left(\theta - \frac{2\pi}{3}\right) & -\sin\left(\theta + \frac{2\pi}{3}\right) \end{bmatrix} \begin{bmatrix} i_A \\ i_B \\ i_C \end{bmatrix} \tag{21}$$

The d - q inductances, L_d and L_q are computed with analytical expressions (12) with Ψ_q and Ψ_d obtained from model simulation considering $\Psi_{PM} = 0$. The estimation of R_c is based on the core losses that depend on the amplitude of flux density B_m in the PMs, rotor and stator (10). Locked-rotor core losses are estimated considering a sinusoidal variation of flux density. So the amplitude of the magnetic flux density, B_m , is computed from estimation of flux distributions B_d and B_q , (22), obtained by stationary simulation of the FE model, with the stator flux aligned with d and q rotor axes and $\Psi_{PM} \neq 0$.

$$B_m = |B_d - B_q| \quad (22)$$

The flux distribution results are also used to evaluate magnetic saturation along with the core. The maximum magnetic flux density is evaluated along the strategic lines of the magnetic circuit (blue lines in Figure 8a). One line crosses the stator teeth in phase A's coil pitch, and another is drawn along the midpoint of the stator outer ring. In the rotor, the average flux density is computed, as the non-uniform flux distribution there makes it difficult to be characterized by a line. If the maximum flux density value in these lines or the average flux density in the rotor is above a defined threshold of $1.6T + 10\%$, the core is considered to violate the magnetic constraint. A 10% tolerance is set to avoid that localized peaks of high flux concentration result in the rejection of a promising geometry during the optimization process. The mesh size considered in the simulation is shown in Figure 8b.

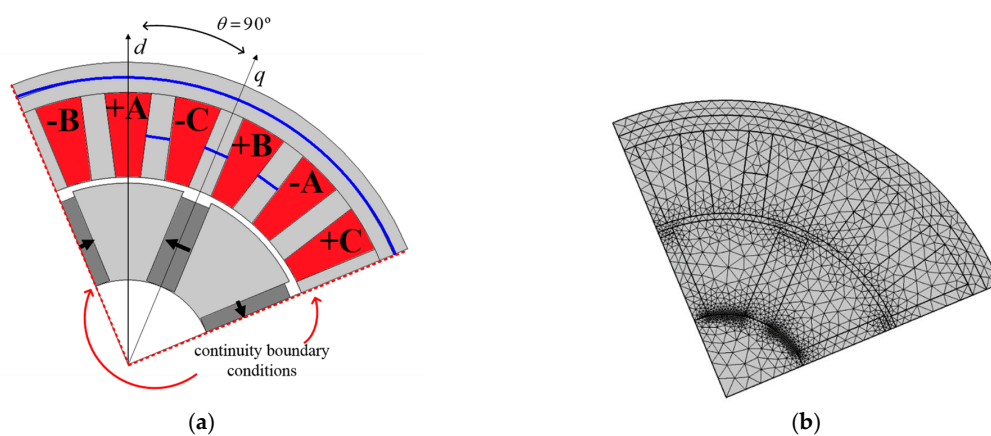


Figure 8. Finite Element Model of an example geometry (a) representation with the rotor's q -axis aligned with phase A and (b) used mesh.

5. Design Optimization

The machine's geometry is optimized to obtain the highest torque and efficiency values while fitting in the available space in the car's suspension system and matching the existent inverter under the thermal safety limitations. To perform the machine design's optimization, the multi-objective genetic algorithm non-dominated sorting genetic algorithm II (NSGA-II) [30], is used, combining the results from the developed FE model and the analytical expressions. This NSGA-II algorithm is chosen because of the multiple physics involved (electromagnetic, thermal, and mechanical phenomena), which are interdependent with non-linear materials, and due to the several constraints present in this application. The NSGA-II is resilient to local optimal points, making it suitable for finding the global minimum of the solution space. The use of optimization tools based on FE models has been proven to be an adequate method for electrical machine design [4–8], when the base FE models are sufficiently fast.

To have an accurate FE model for the machine's performance and, at the same time, a fast-computational method to be used in the NSGA-II tool, the FE model is simulated using a stationary time reference for the d - q axes, to compute the machine's inductances, losses, and magnetic saturation. These parameters are then used by an auxiliary script to estimate the machine's performance,

using Equations (3) to (19). This integration between the FE and analytical models allow the fast estimation of the machine’s performance with sufficiently high accuracy.

In Figure 9 the flowchart of the optimization algorithm is shown. The NSGA-II generates a population of individuals, where each is described by an optimization vector x , called decision variables. Each objective function and constraints are evaluated with the presented electromagnetic and thermal models, as shown in Figure 10.

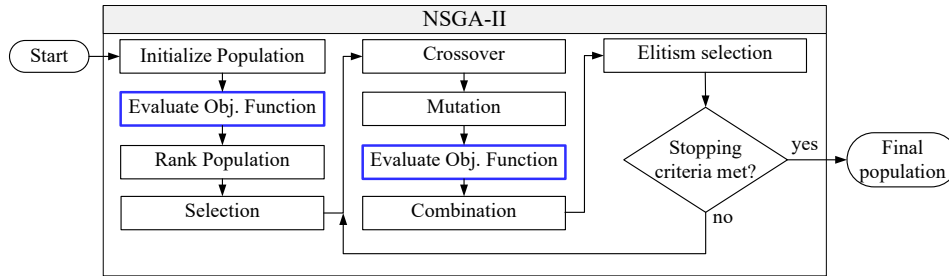


Figure 9. Non-dominated sorting genetic algorithm II (NSGA-II) process flowchart.

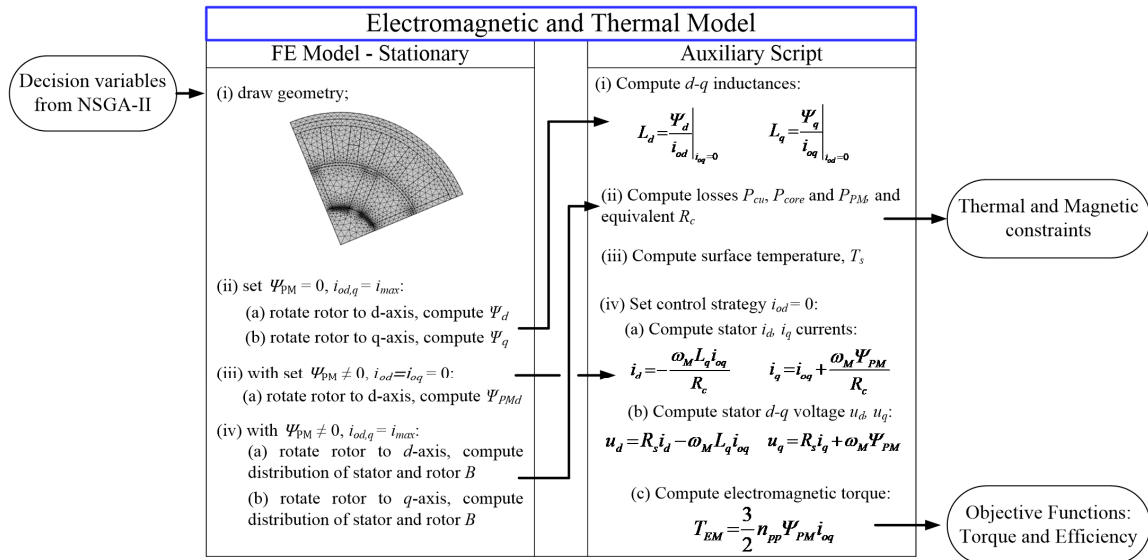


Figure 10. Objective function evaluation.

5.1. Objective Functions

The main goals of the optimization are to maximize the produced torque and efficiency, without saturating the magnetic core or exceeding the material’s withstanding temperature. As such, the objective functions are the electromagnetic torque, $f_1 = T_{EM}$, and efficiency, $f_2 = \eta$, (23)–(25). The electromagnetic component of the generated torque was chosen to be optimized as it gives a good indication of the total torque of the machine, and it simplifies the machine’s model equations, thus reducing its computational time. With $i_{od} = 0A$ one obtains (26)–(29), which only needs the computation of one inductance, L_q .

$$\max_{x \in \Omega} (f_1(x), f_2(x)) \tag{23}$$

$$f_1 = T_{EM} = \frac{3}{2} n_{pp} \Psi_{PM} i_{oq} \tag{24}$$

$$f_2 = \eta = \frac{T_{EM} \omega_M}{T_{EM} \omega_M + p_{core} V_{core} + \rho_{PM} V_{PM}} \tag{25}$$

$$v_d = R_s i_d - \omega_M L_q i_{oq} \tag{26}$$

$$v_q = R_s i_q + \omega_M \Psi_{PM} \quad (27)$$

$$i_d = -\frac{\omega_M L_q i_{oq}}{R_c} \quad (28)$$

$$i_q = i_{oq} + \frac{\omega_M \Psi_{PM}}{R_c} \quad (29)$$

5.2. Decision Variables

Decision variables are the set of parameters that defines a unique machine design according to the presented 2D geometry model. These variables, presented in Figure 5, were set with the ranges given in Table 6, according to the available space for the machine. In addition to the geometric characteristics, the torque producing current density, J_{oq} , is also optimized by the NSGA-II, to account for temperature constraints.

Table 6. Optimization decision variables.

Variable	Description	Range
r_r	Rotor radius	20–40 mm
w_s	Stator outer ring width	1–20 mm
w_m	Magnet width	1–7 mm
l_m	Magnet length	5–15 mm
w_t	Teeth width	1–10 mm
l_t	Teeth length	7–20 mm
g	Airgap size	1–5 mm
r_s	Shaft radius	5–30 mm
J_{oq}	Torque producing current density (q axis)	1–60 A/mm ²

5.3. Constraints

Constraints must be set according to the defined requirements to ensure the feasibility of the machine with the optimized geometry. Geometrical constraints limit the machine's dimension to the available space near the wheels of the vehicle and its maximum weight. Thermal constraints limit operating temperature, protecting the permanent magnets and winding isolation (H class insulation) according to the respective material's limits. A constraint on the maximum magnetic flux density is also set to avoid saturation of the machine's core, leading to less efficiency operation points and, therefore, computing unnecessary low-efficiency geometries. These constraints and respective ranges are presented in Table 7.

Table 7. Optimization constraints by type and respective ranges.

Constraint Type	Constraint	Range
Geometrical	Weight	<5 kg
	Stator outer radius	<50 mm
	Motor stack length	=80 mm
Thermal	PM's maximum temperature	<120 °C
	Windings temperature	<180 °C
Magnetic	Magnetic flux density	<1.6T + 10%

5.4. Optimization Results

The optimization was done in 22.9 h, using a population of 150 elements and 150 generations, defined empirically based on a set of previous tests. Figure 11 shows the final Pareto front obtained, for the maximization of the torque and efficiency. All solutions of the Pareto front meet the thermal

and magnetic constraints. As can be seen, the efficiency decreases with the increase of the torque. For the previously specified torque requirement (each IPMSM should have at least a torque of 20 Nm), its Pareto front point is identified in Figure 11 by a red “O”. For the required torque of 20 Nm, the corresponding electrical efficiency is 98,6%, accounting for the copper, magnetic core, and PM losses. To understand the characteristics of the machine, in Figure 12 the objective functions and decision variables for each population element are shown, sorted by the lowest to the higher torque value. The population element number 57 corresponds to the desired solution with $T = 20$ Nm. This is marked by a red “O” in each figure. Figure 12a shows that, as a result of the optimization process, increasing the torque reduces the machine’s efficiency, and vice-versa. This is due to the mechanical, magnetic, and thermal constraints. As the maximum size of the machine is fixed, increasing the torque can be done by increasing the current density, Figure 12b, and the stator tooth width, w_t , Figure 12e, that will increase the windings and core losses and, thus, reducing the efficiency. From the figures analysis it is also important to state that the magnets size rapidly reach their maximum values due to geometrical constraints (w_m and l_m in Figure 12d).

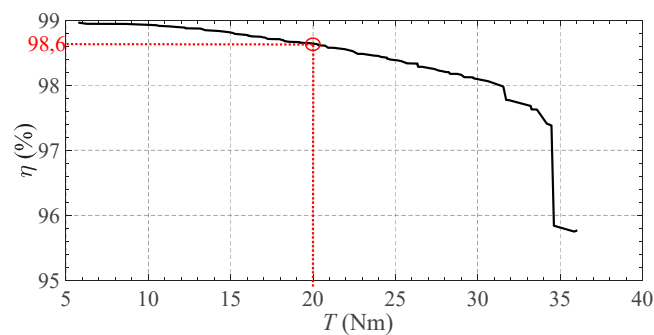


Figure 11. Pareto front—Objective functions.

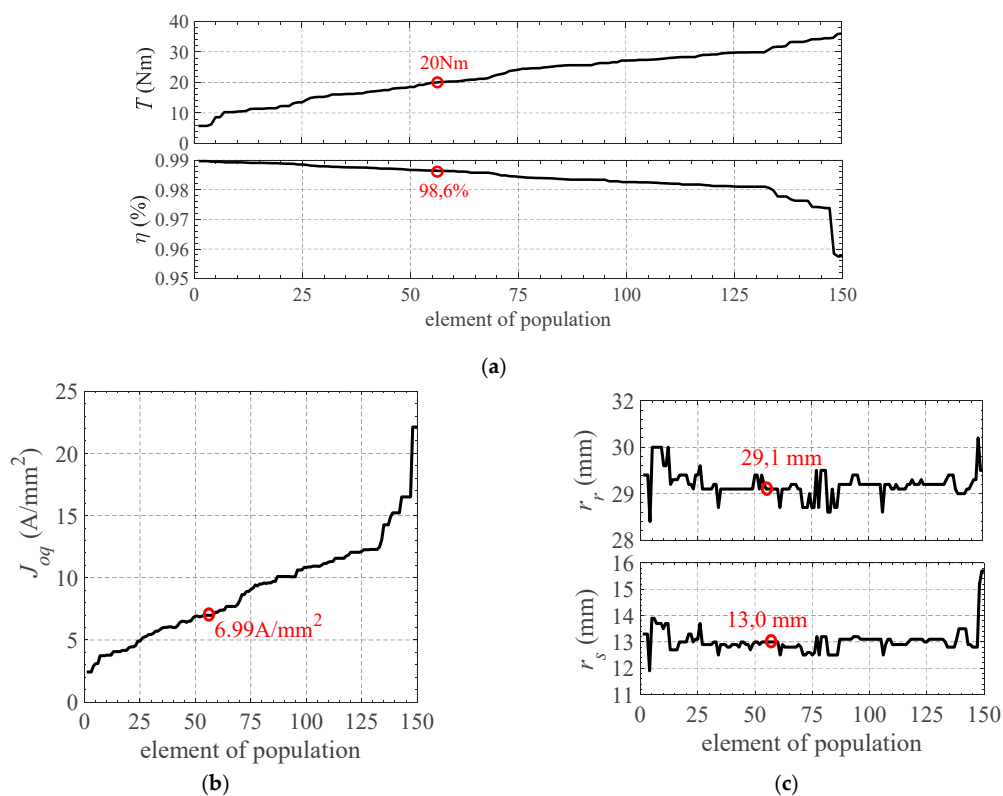


Figure 12. Cont.

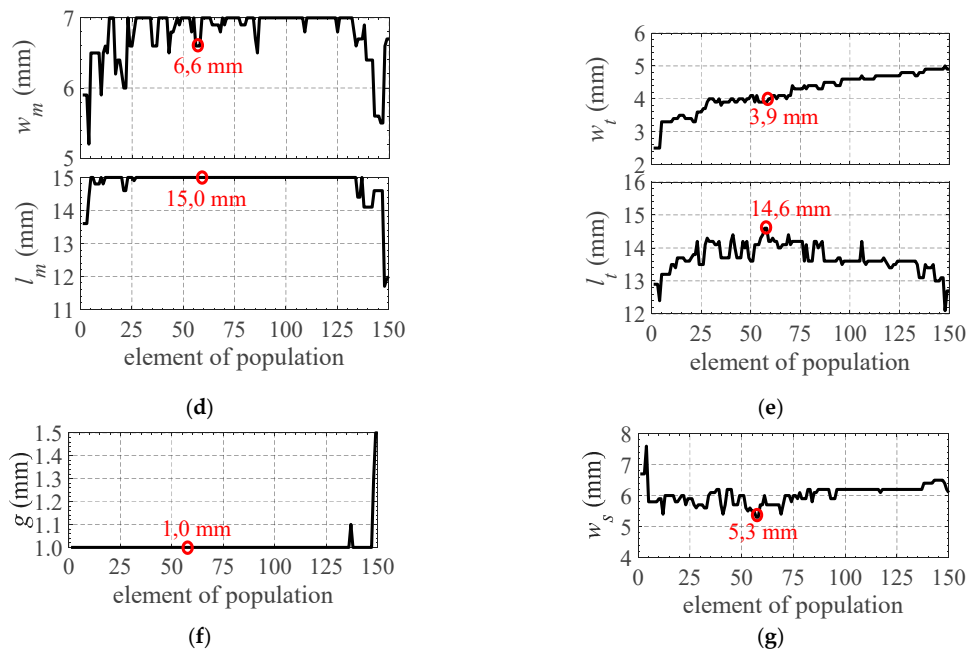


Figure 12. Pareto front—Objective functions and decision variables. In each figure is shown the evolution, for each element of population, of (a) the torque, T , and efficiency, η , (b) the torque producing current density, J_{oq} , (c) the rotor and shaft radius, r_r and r_s , (d) the magnet width and length, w_m and l_m , (e) the teeth width and length, w_t and l_t , (f) the airgap size, g , and (g) the stator outer ring width, w_s .

To understand which constraint is limiting the machine torque, the torque producing current density amplitude, J_{oq} , and maximum value of the magnetic flux density, B , inside the machine are shown for all elements of the population, Figure 13. As can be seen in Figure 13a, the optimal torque producing current density is below its maximum thermal value, J_{Th} , thus existing a thermal safety margin. Besides, the stator current density, J , is almost the same as the torque producing current, J_{oq} , meaning that the contribution from magnetic core and PM losses is minimal. The IPMSM's torque is, thus, limited by the maximum magnetic flux density, $B = 1.6T + 10\%$, Figure 13b. Please note that this value will only occur in some parts of the machine's magnetic core. This is seen for all elements of the population. For the chosen optimal point ($T = 20$ Nm), with a maximum allowed thermal current density, J_{Th} , of 20.08 A/mm² and a torque producing current density, J_{oq} , of 6.99 A/mm², the water cooling system can be redesigned for a small heat transfer coefficient (or keeping the same geometry with lower water flow).

The final dimensions and current density for the optimized solution are listed in Table 8. In Figure 14a it is drawn to a 2D cross-section of the optimized IPMSM, in Figure 14b, the distribution of the magnetic field along the IPMSM with the rotor aligned with the q -axis, to produce the nominal torque of 20 Nm, and in Figure 14c is a 3D sketch.

The selected optimized solution is further analyzed to estimate the IPMSM performance. The number of stator windings turns 20 to achieve the desired voltage/speed characteristic of around 8000 rpm base speed at 380 V, the inverter's maximum voltage. The permanent magnet linked flux, Ψ_{PM} , and d - q linked fluxes Ψ_d , Ψ_q are calculated with the FE model, considering cross-saturation from which L_d and L_q maps are determined from (11) and (12), Figure 15.

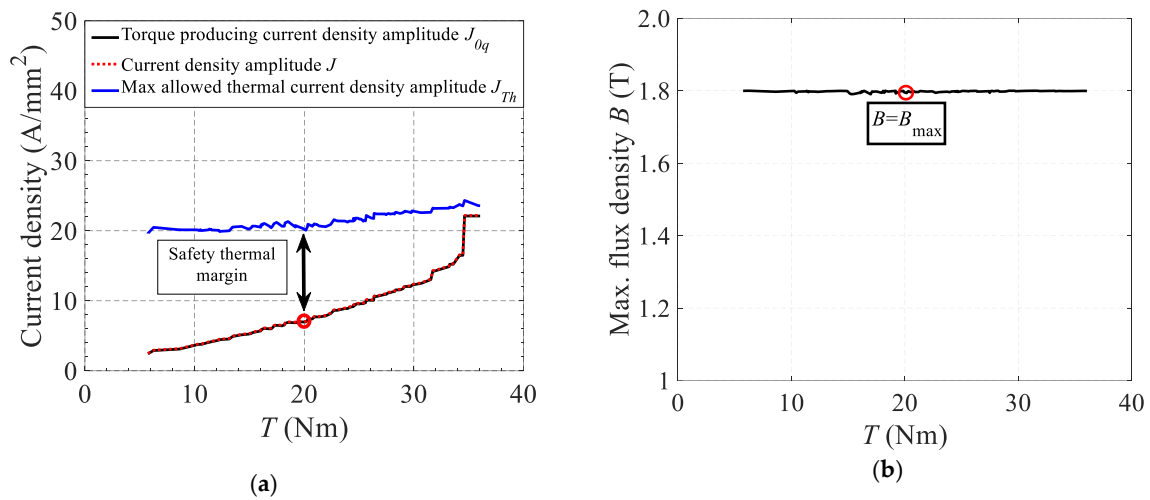


Figure 13. Current density and magnetic flux density. In (a) the torque producing current density J_{oq} , the current density, J , and the maximum allowed thermal current density, J_{Th} , as a function of the torque, T , and in (b) the maximum value of flux density, B , as a function of the torque, T .

Table 8. Optimization decision variables.

Variable	Description	Optimized Solutions
r_r	Rotor radius	29.0 mm
w_s	Stator outer ring width	5.3 mm
w_m	Magnet width	6.6 mm
l_m	Magnet length	15.0 mm
w_t	Teeth width	3.9 mm
l_t	Teeth length	14.6 mm
g	Airgap size	1.0 mm
r_s	Shaft radius	13 mm
J_{oq}	Torque producing current density (q -axis)	6.99 A/mm ²

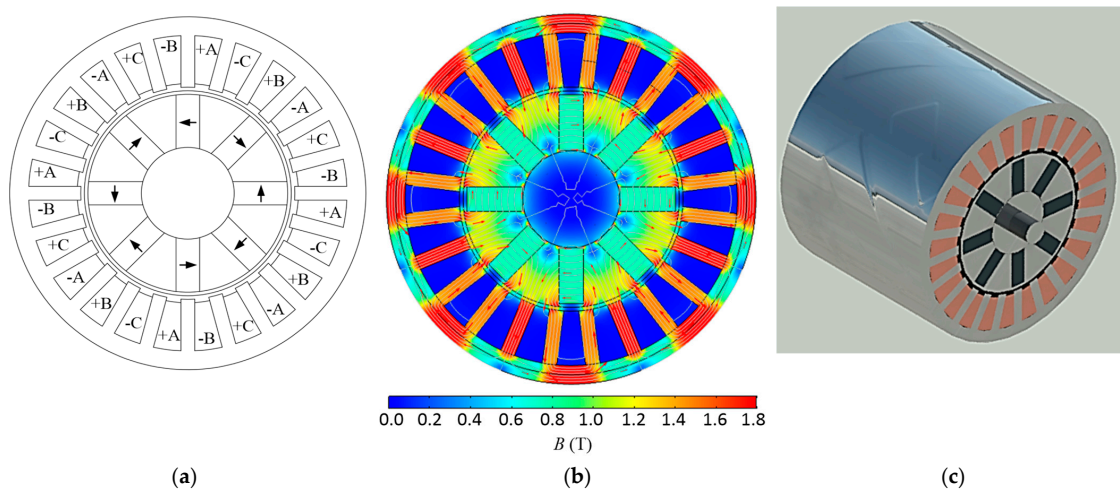


Figure 14. Optimized solution for 20 Nm: (a) geometry, (b) distribution of magnetic flux density, and (c) 3D geometry.

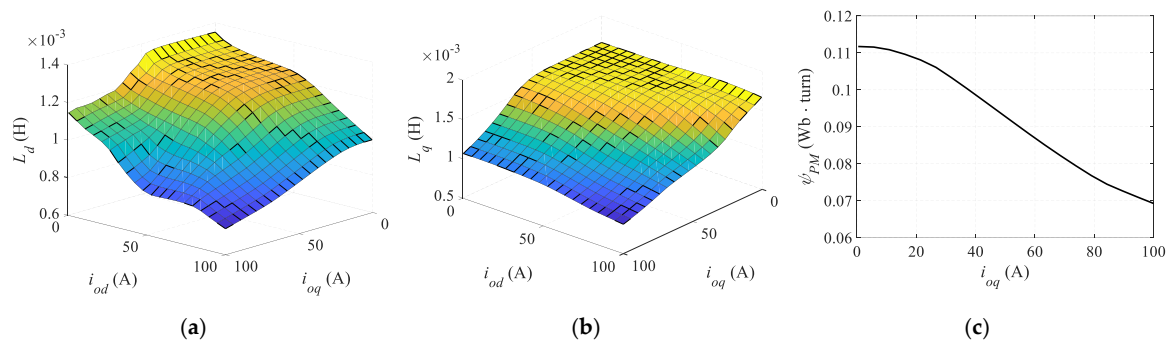


Figure 15. Optimized solution's induction coefficients (a) L_d , (b) L_q , and (c) permanent magnet linked flux Ψ_{PM} .

The torque map is estimated from these with (5) limited to the optimum torque producing current density $J_{oq} = 6.99 \text{ MA/m}^2$ ($I = 33 \text{ A}$), corresponding to the required 20 Nm, Figure 16a. In this case, the efficiency map, Figure 16b is obtained for the operation points following the maximum torque per ampere (MTPA) strategy from (3)–(7). These points are presented in Figure 16a representing the constant torque and field weakening regions. The MTPA trajectory on the constant torque region shows small $I_d = 5 \text{ A}$ at 20 Nm, meaning that reluctance torque is not a considerable component. This stems from the optimization being based on the maximization of the electromagnetic torque component. As seen in Figure 16b the field weakening region occurs from 8000 rpm onwards.

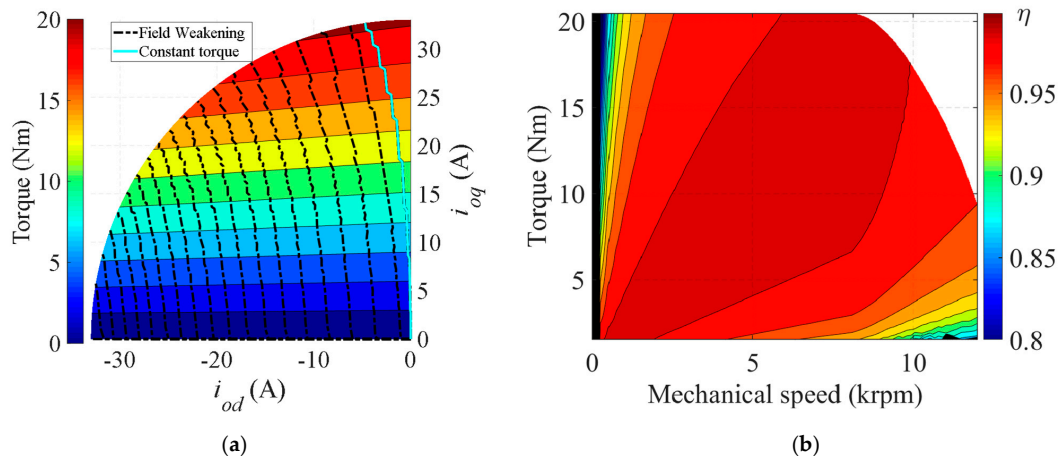


Figure 16. Optimized solution's performance: (a) torque map and (b) efficiency map.

6. Prototype Design Analysis

The optimized geometry was obtained using a simplified geometry model and considering mainly geometrical and thermal constraints. However, there are mechanical requirements and manufacturing cost limitations to be considered that lead to changes in this design so that the motor can be built. The final design is presented along with experimental analysis of its electromagnetic and thermal characteristics that validate the set requirements.

6.1. Final Design

Changes were made to the rotor and shaft geometry, so these can bear the centrifugal mechanical stresses caused by rotation speed and torque in normal and faulty operation. The shaft design was changed with the introduction of fins (with 1.5mm width) to assure an effective torque transmission between the rotor magnetic core and the shaft, Figure 17a). Shaft fins contribute to holding the rotor

core at high rotational speed, avoiding deformation or detachment. They also allow the distribution of the resulting mechanical efforts equally between each pole region.

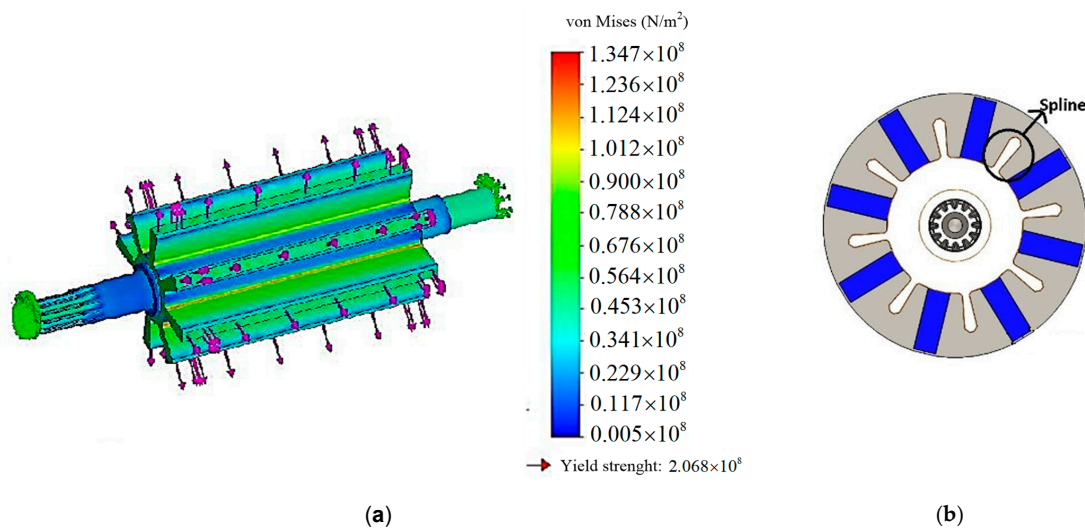


Figure 17. Shaft and rotor designs: (a) final shaft design and (b) ultimate rotor's magnetic circuit.

The maximum tensile strength obtained for the machine operating point was 206.8 MPa, lower than the withstand value of 290 MPa. Therefore, splines were cut in the rotor's magnetic core, Figure 17b, where the shaft fins are inserted. This part of the machine is not magnetic as the shaft is made of stainless steel, being adopted to allow the machine to be as compact as possible due to the limitations of space available at the vehicle's wheels. Of course, with the change in the rotor magnetic core, a difference is expected in the rated torque, which will be seen in the experimental results. The final motor design is presented in Figure 18. The obtained optimized design was built and assembled, weighing a total of 5.05 kg, including a cooling jacket and housing.

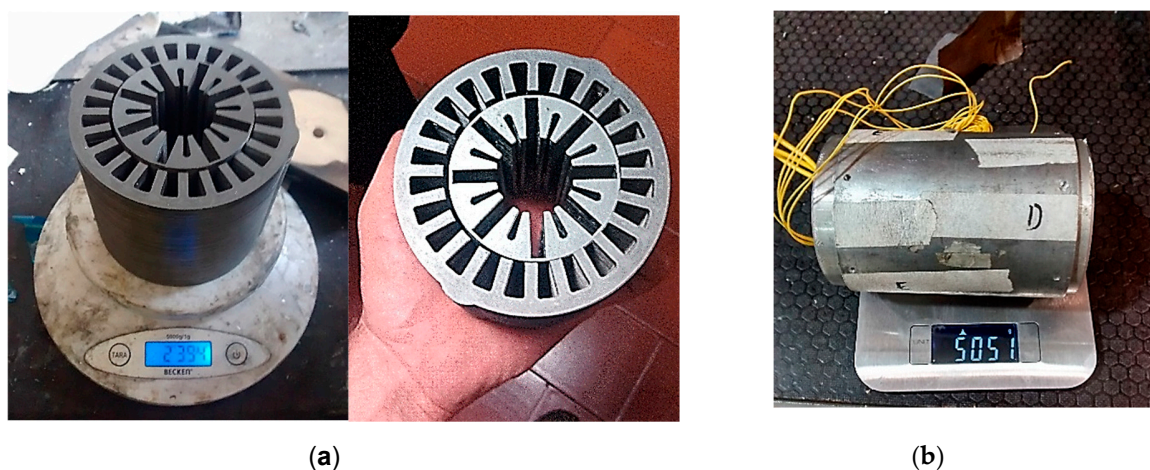


Figure 18. Final motor prototype: (a) magnetic circuit, (b) assembled prototype.

6.2. Experimental Tests

To validate the performance of the prototype experimentally, the torque and efficiency maps were calculated based on preliminary tests. A test bench composed of the developed IPMSM prototype coupled with an existing 35 kW 5000 rpm PMSM with a transmission box system with ratios of 4:1 and 1:20 was established, Figure 19. Each machine is connected to one inverter. The prototype's inverter is supplied by a 600 V voltage source, and the load generator's inverter is connected to a 600 V battery.

Both inverters are connected to individual controllers. In Figure 20 the overall diagram of the testbench is shown.

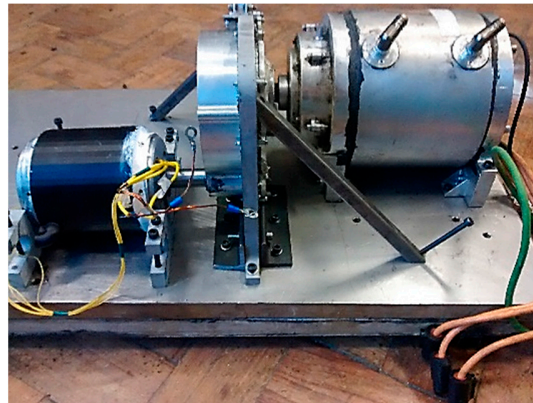


Figure 19. Test bench configuration with the prototype (left side) and Siemens motor (right side) mechanically coupled through a transmission gear.

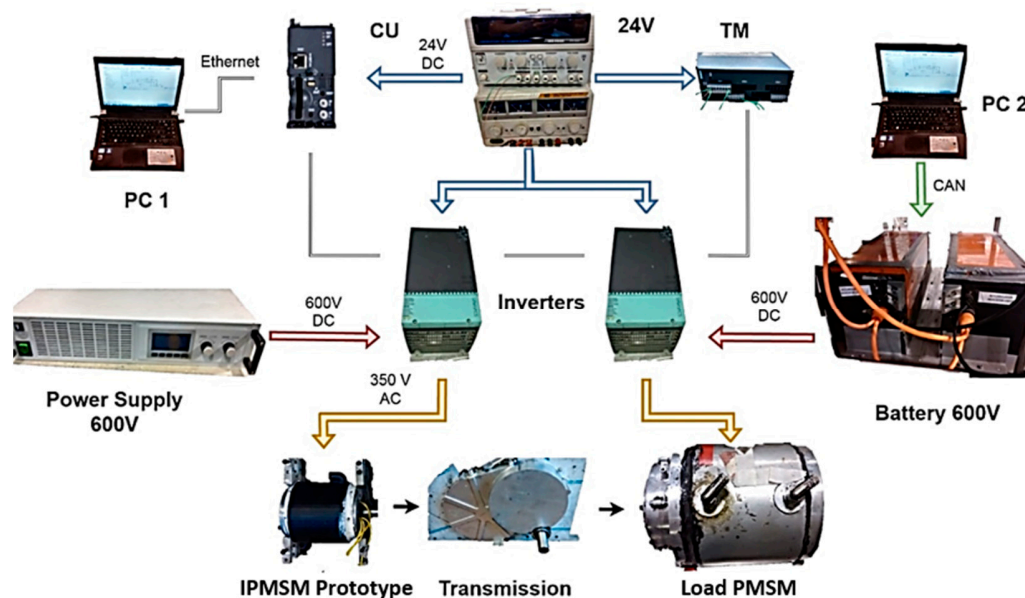


Figure 20. Overall diagram of the working testbench.

By limiting the current to its maximum value and using a field-oriented control strategy for the developed IPMSM, with $I_d = 0$ A, the torque and speed of the machine were changed and registered. The efficiency of the motor was estimated by measuring the output torque of the IPMSM and the required input power. In Table 9 the experimental values obtained for each operation point are shown. These values are then used to construct Figure 21 using a linear 2D interpolation method between experimental points. Due to limitations of the load PMSM, it was not possible to obtain more results in the field weakening region.

From experimental results, it verified that the torque produced for the rated current was 18.2 Nm, a reduction of about 9% from the expected one (20 Nm). Additionally, the IPMSM efficiency was about 90%, a significant decrease from the expected 98.6%. The reduction of torque was anticipated due to the modifications made to the final design to facilitate the manufacturing process. However, its decline is acceptable for the application, as discussed in next section “estimated track performance”. The reduction of efficiency was substantial because of several aspects not considered during the simulation: (1) the friction losses in the bearing were not considered and are taken into account in the

experimental tests (torque was measured in the shaft using a torque meter); (2) the harmonic content from the inverter's commutations were not considered; (3) the border effects were not found (it was used a 2D FE model instead of a 3D FE model); (4) the modifications made to the final prototype were not included. From these, the use of a 2D FE model instead of a 3D one can have a considerable impact as it leads to an overestimation of the magnetic flux density, and consequently torque, in electrical machines, as shown in [31], where a 6% difference was registered between the flux density distribution in the airgap obtained with a 2D and 3D FE model.

Two tests, 30 min long, were conducted to evaluate not only, reliability, but mainly, the temperatures of the motor with and without water refrigeration at the nominal current. The initial temperatures of both tests were around 25 °C, and the flow rate of the cooling pump was 17 l/min. The experimental temperature, shown in Figure 22 was measured inside phase A of the windings using a temperature sensor. Due to the reduction of efficiency, the experimental temperature of around 73 °C was higher than the simulated one. However, this does not constitute a problem because it is still lower than the materials withstanding temperature (remember that the optimized simulated solution had a very high-temperature safety margin).

Table 9. Torque, speed, and efficiency map of the developed prototype.

Torque (Nm)	Speed (krpm)												
	0.5	1	2	3	4	5	6	7	8	9	10	11	12
1.8	0.52	0.55	0.57	0.60	0.61	0.63	0.66	0.70	0.68	0.67	0.65	0.6	0.58
3.6	0.46	0.54	0.59	0.60	0.65	0.67	0.71	0.72	0.73	0.75	0.73	0.72	-
5.5	0.44	0.53	0.62	0.70	0.73	0.76	0.80	0.81	0.82	0.85	0.86	-	-
7.3	0.43	0.56	0.65	0.75	0.76	0.80	0.82	0.88	0.91	0.92	-	-	-
10.9	0.42	0.62	0.72	0.79	0.81	0.83	0.84	0.86	0.93	0.94	-	-	-
14.5	0.42	0.52	0.73	0.73	0.74	0.76	0.80	0.85	0.90	0.92	-	-	-
18.2	0.37	0.52	0.66	0.68	0.68	0.69	0.75	0.80	0.85	0.90	-	-	-

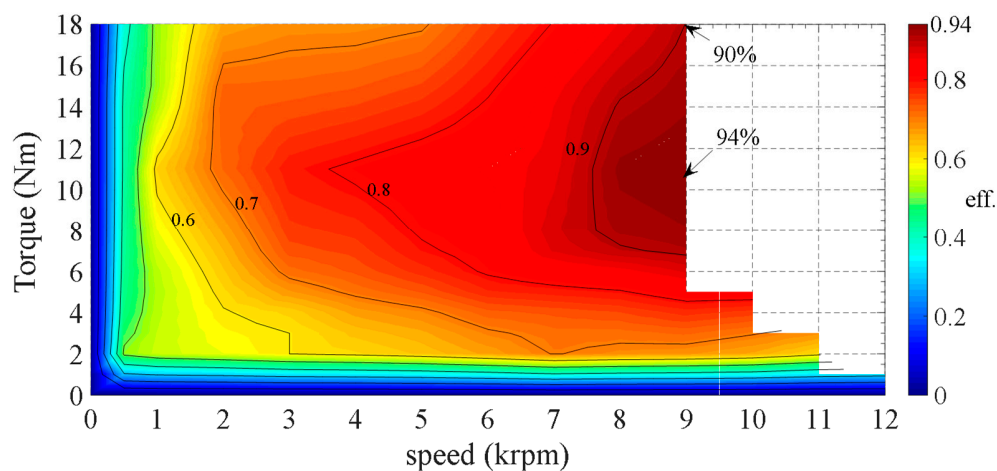


Figure 21. Experimentally estimated efficiency map.

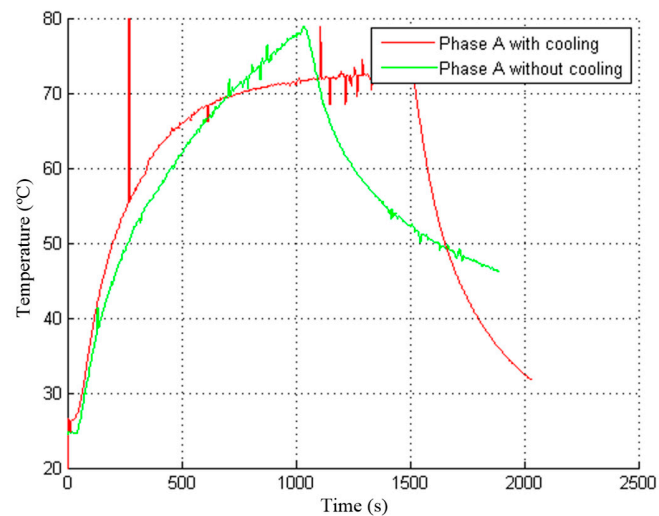


Figure 22. Experimental temperature with the nominal current.

6.3. Estimated Track Performance

From experimental results, it can be concluded that the nominal torque and power of the developed IPMSM prototype are 18.2 N and 17.2 kW. Combining the four IPMSM, to be installed at each wheel, the powertrain expected nominal torque and power are 72.8 Nm and 68.8 kW, respectively. The track simulation was done now using the characteristics of the prototype. The power and torque developed along the track are shown in Figures 23–25. With these, for each configuration, the peak speed velocities during the track were 80.8 km/h and 78.3 km/h, and the times to complete one lap were 77.3 s and 78.9 s. The difference between these values is small because, during high speeds, the aerodynamic forces are predominant, and a reduction of around 9% in the available torque does not produce a linear decrease of the speed. The main difference between the performances of the ideal optimized motor and the prototyped one is related to the motor losses. As seen in Figure 25, despite producing different output powers, the required motor's input powers are very similar. The energy consumptions are 1.19 kWh and 1.14 kWh for the ideal and prototyped motors. Therefore, using about the same energy, a decrease of output power and, consequently, an increase of 2.1% in the lap time is expected for the prototyped motor, due to its lower efficiency and torque. Despite this time lap increase, the prototyped motor successfully reached the target performance.

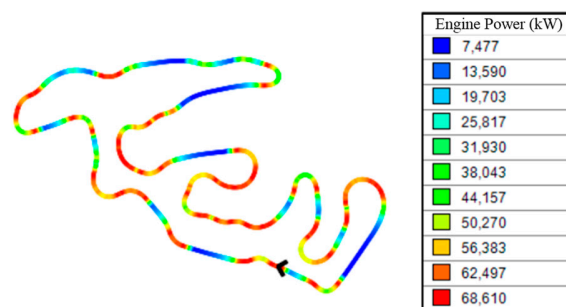


Figure 23. Optimal power developed along the FSAE autocross Germany track for the characteristics of the prototyped motor.

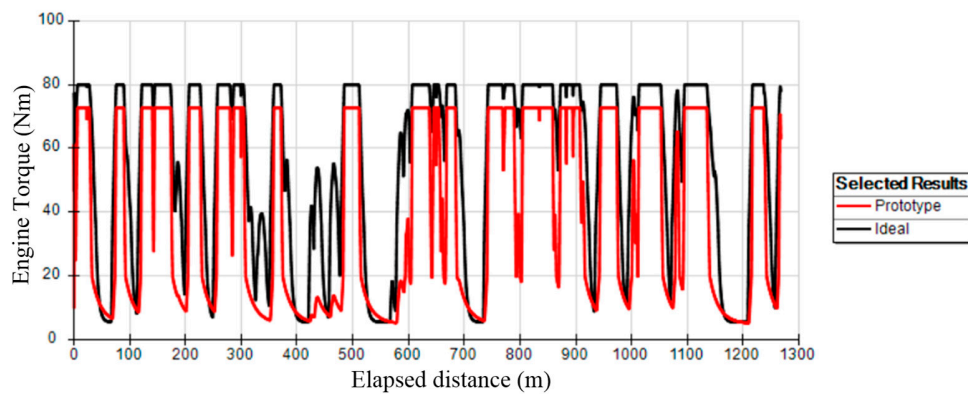


Figure 24. Optimal torque developed along the FSAE Autocross Germany track for the characteristics of the ideal optimized motor and the prototyped motor.

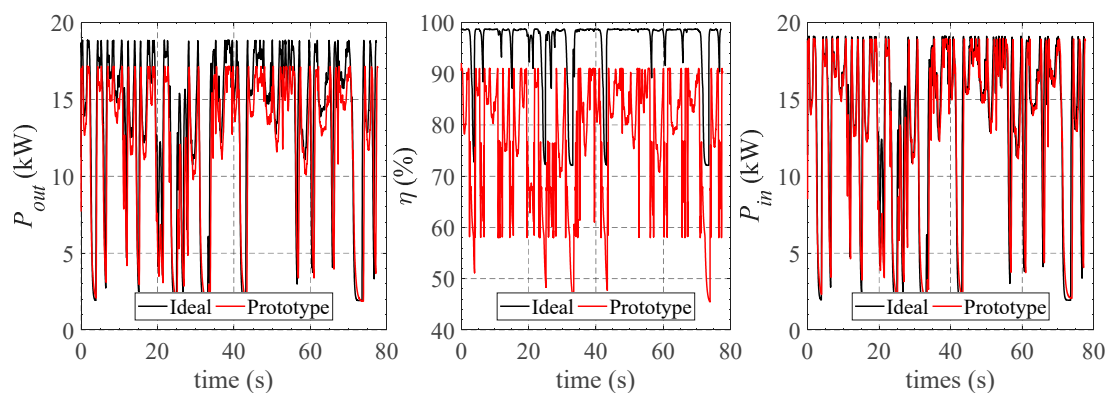


Figure 25. Motor output power, P_{out} , efficiency, η , and input power, P_{in} , along the FSAE Autocross Germany track for the ideal optimized motor and the prototyped motor.

7. Conclusions

This work focuses on the design, optimization, and prototyping of a 20 kW 8000 rpm permanent magnet synchronous motor for the electric vehicle of FormulaStudent (FST) competitions, considering a typical driving cycle. Due to the multiple number of physics, variables, and constraints and the non-linearity of materials, the optimization of the motor was done using a genetic algorithm: non-dominated sorting genetic algorithm II (NSGA-II). The use of this algorithm allows the visualization of the Pareto front and the analysis of the different motor variables along with the optimized solutions. To have a sufficiently accurate electromagnetic and thermal model and, at the same time, a feasible time for the optimization process, a hybrid analytical/FE model was developed. The hybrid model is composed of a stationary time 2D finite element model, to calculate the motor's main parameters, as d - q inductances, permanent magnet flux distribution, and losses, and an auxiliary script to compute analytically the voltage, torque, and efficiency curves.

The required nominal power and speed for the FST electric vehicle were estimated using the auxiliary software OptimumLap (version 1.5.5, OptimumG, Centennial, CO, USA) by optimizing the driving cycle on the FSAE Autocross Germany track, with a maximum torque of 80 Nm for the vehicle powertrain (a constraint defined in FST competitions). From the optimization of the driving cycle and using a motor at each wheel of the vehicle, a target of 20 Nm, 20 kW, and 8000 rpm was defined for each motor as nominal values. The motor's optimization was done in 22.9 h, using a population of 150 elements and 150 generations, i.e., 22,500 different motor geometries were tested. This was done in a feasible time due to the low computational time of developed electromagnetic and thermal models, about 3.66 s per simulation. From the Pareto front (optimized results) it was possible to obtain a motor design with 20 Nm and 98.6% of efficiency. By the analysis of each decision variable, it is concluded

that the motor's performance is limited by the saturation curve of the ferromagnetic material. However, due to its water-cooling system, it has a high thermal safety margin. This thermal safety margin was revealed to be important because, due to changes included in the final prototype design, the final motor losses increased.

The optimized motor was built and tested in a laboratorial environment. Due to mechanical aspects, some changes were included in its design, which, alongside with the deviations resultant from using a 2D model instead of a 3D one, contributed to the decrease of the motor's torque and efficiency. It was registered an experimental nominal torque and efficiency of 18.2 Nm and 90% for the developed prototype. To analyze the impact of the torque and efficiency reduction in the vehicle performance, both ideal optimized motor and prototyped one was included in the auxiliary software OptimumLap to compute the optimal driving cycles. As a result, despite requiring about the same energy per lap, the prototyped motor led to an increase of time lap of 2.1%, when compared with the ideal optimized motor.

Author Contributions: Conceptualization, methodology and software: P.P.C.B. and J.G.S.; validation and formal analysis: P.P.C.B., J.G.S., J.F.P.F., P.J.C.B.; writing—original draft preparation, writing—review and editing, P.P.C.B., J.F.P.F., P.J.C.B.; supervision, J.F.P.F., P.J.C.B. All authors have read and agreed to the published version of the manuscript.

Funding: This research received no external funding.

Acknowledgments: This work was supported by FCT—Foundation for Science and Technology, I.P., through IDMEC, under LAETA, project UIDB/50022/2020.

Conflicts of Interest: The authors declare no conflict of interest.

References

1. Yang, Z.; Shang, F.; Brown, I.P.; Krishnamurthy, M. Comparative Study of Interior Permanent Magnet, Induction, and Switched Reluctance Motor Drives for EV and HEV Applications. *IEEE Trans. Transp. Electr.* **2015**, *1*, 245–254. [[CrossRef](#)]
2. Pellegrino, G.; Vagati, A.; Boazzo, B.; Guglielmi, P. Comparison of Induction and PM Synchronous Motor Drives for EV Application Including Design Examples. *IEEE Trans. Ind. Appl.* **2012**, *48*, 2322–2332. [[CrossRef](#)]
3. Widmer, J.D.; Martin, R.; Kimiabeigi, M. Electric Vehicle Traction Motors without Rare Earth Magnets. *Sustain. Mater. Technol.* **2015**, *3*, 7–13. [[CrossRef](#)]
4. Vaimann, T.; Kallaste, A.; Kilk, A. Magnetic Properties of Reduced Dy NdFeB Permanent Magnets and Their Usage in Electrical Machines. In Proceedings of the 2013 Africon, Pointe-Aux-Piments, Mauritius, 9–12 September 2013; pp. 1–5.
5. Ge, X.; Zhu, Z.Q.; Li, J.; Chen, J. A Spoke-Type IPM Machine with Novel Alternate Airspace Barriers and Reduction of Unipolar Leakage Flux by Step-Staggered Rotor. *IEEE Trans. Ind. Appl.* **2016**, *52*, 4789–4797. [[CrossRef](#)]
6. Lee, B.; Kang, G.; Hur, J.; Member, S.; You, D. Design of Spoke Type BLDC Motors with High Power Density for Traction Applications. In Proceedings of the Conference Record of the 2004 IEEE Industry Applications Conference, 2004 39th IAS Annual Meeting, Seattle, WA, USA, 3–7 October 2004; Volume 2, pp. 1068–1074.
7. Hwang, K.Y.; Jo, J.H.; Kwon, B.I. A Study on Optimal Pole Design of Spoke-Type Ipmsm with Concentrated Winding for Reducing the Torque Ripple by Experiment Design Method. *IEEE Trans. Magn.* **2009**, *45*, 4712–4715. [[CrossRef](#)]
8. Han, W.; van Dang, C.; Kim, J.; Kim, Y.; Jung, S. Global-Simplex Optimization Algorithm Applied to FEM-Based Optimal Design of Electric Machine. *IEEE Trans. Magn.* **2017**, *53*, 1–4. [[CrossRef](#)]
9. Jung, S.; Ro, J.; Jung, H. A Hybrid Algorithm Using Shape and Topology Optimization for the Design of Electric Machines. *IEEE Trans. Magn.* **2018**, *54*, 1–4. [[CrossRef](#)]
10. Bhagubai, P.; João, F.P. Fernandes, Multi-objective Optimization of Electrical Machine Magnetic Core using a Vanadium-Cobalt-Iron alloy. *IEEE Trans. Magn.* **2020**, *56*, 1–9. [[CrossRef](#)]
11. Huynh, T.A.; Hsieh, M.-F. Performance Analysis of Permanent Magnet Motors for Electric Vehicles (EV) Traction Considering Driving Cycles. *Energies* **2018**, *11*, 1385. [[CrossRef](#)]

12. Risticvic, M.; Iles, D.; Moeckel, A. Design of an Interior Permanent Magnet Synchronous Motor Supported by the Topology Optimization Algorithm. In Proceedings of the 2016 International Symposium on Power Electronics, Electrical Drives, Automation and Motion (SPEEDAM), Anacapri, Italy, 22–24 June 2016; pp. 221–225.
13. Bianchi, N.; Bolognani, S. Design Optimisation of Electric Motors by Genetic Algorithms. *IEE Proc. Electr. Power Appl.* **1998**, *145*, 475–483. [CrossRef]
14. OptimumG, LLC. OptimumLap, Version 1.5.5. Available online: <https://optimumg.com/product/optimumlap/> (accessed on 26 February 2020).
15. Chan, K.T.; Chau, C.C. *Modern Electric Vehicle Technology*; Oxford University Press: Oxford, UK, 2001.
16. Krings, A.; Cossale, M.; Tenconi, A.; Soulard, J.; Cavagnino, A.; Boglietti, A. Magnetic Materials Used in Electrical Machines: A Comparison and Selection Guide for Early Machine Design. *IEEE Ind. Appl. Magn.* **2017**, *23*, 21–28. [CrossRef]
17. Cogent Surahammars Bruks AB, “NO20 Datasheet”. Available online: https://cogent-power.com/cms-data/downloads/Hi-Lite_NO20.pdf (accessed on 10 January 2020).
18. Slemmon, G.R.; Gumaste, V. Steady-State Analysis of a Permanent Magnet Synchronous Motor Drive with Current Source Inverter. *IEEE Trans. Ind. Appl.* **1983**, *IA-19*, 190–197. [CrossRef]
19. AISI Type 316 Stainless Steel, Annealed Bar. Available online: <http://asm.matweb.com/search/SpecificMaterial.asp?bassnum=MQ316J> (accessed on 10 January 2020).
20. TDK Corporation, “Neodymium Magnets NEOREC Series.” Issued in May 2011. Available online: https://product.tdk.com/en/search/magnet/magnet/neodymium/info?part_no=NEOREC45SH (accessed on 10 January 2020).
21. Smith, S.; Delgado, D. Automated AC Winding Design. In Proceedings of the 5th IET International Conference on Power Electronics, Machines and Drives (PEMD 2010), Brighton, UK, 19–21 April 2010.
22. Lee, J.-Y.; Lee, S.-H.; Lee, G.-H.; Hong, J.-P.; Hur, J. Determination of Parameters Considering Magnetic Nonlinearity in an Interior Permanent Magnet Synchronous Motor. *IEEE Trans. Magn.* **2006**, *42*, 1303–1306.
23. Yamazaki, K.; Fukuoka, T.; Akatsu, K.; Nakao, N.; Ruderman, A. Investigation of Locked Rotor Test for Estimation of Magnet PWM Carrier Eddy Current Loss in Synchronous Machines. *IEEE Trans. Magn.* **2012**, *48*, 3327–3330. [CrossRef]
24. Han, S.; Jahns, T.M.; Zhu, Z.Q. Analysis of Rotor Core Eddy-Current Losses in Interior Permanent Magnet Synchronous Machines. In Proceedings of the 2008 IEEE Industry Applications Society Annual Meeting, Edmonton, AB, Canada, 5–9 October 2008; pp. 1–8.
25. Huang, W.; Bettayeb, A.; Kaczmarek, R.; Vannier, J. Optimization of Magnet Segmentation for Reduction of Eddy-Current Losses in Permanent Magnet Synchronous Machine. *IEEE Trans. Energy Convers.* **2010**, *25*, 381–387. [CrossRef]
26. Mateev, V.; Marinova, I. Loss Estimation of Magnetic Gears. *Electr. Eng.* **2020**, *102*, 387–399. [CrossRef]
27. Fontes, P.M.d.A. Cooling System of FormulaStudent Electric Motor” (“Refrigeração do Propulsor Elétrico de um Veículo Formula Student. Master’s Thesis, Instituto Superior Técnico, Lisboa, Portugal, 2016; pp. 1–102.
28. Popescu, M.; Staton, D.; Boglietti, A.; Cavagnino, A.; Hawkins, D.; Goss, J. Modern Heat Extraction Systems for Electrical Machines—A Review. In Proceedings of the 2015 IEEE Workshop on Electrical Machines Design, Control and Diagnosis (WEMDCD), Torino, Italy, 26–27 March 2015; pp. 289–296.
29. Fénot, M.; Bertin, Y.; Dorignac, E.; Lalizel, G. A Review of Heat Transfer between Concentric Rotating Cylinders with or without Axial Flow. *Int. J. Therm. Sci.* **2011**, *50*, 1138–1155. [CrossRef]
30. KDeb, K.; Pratap, A.; Agarwal, S.; Meyarivan, T. A Fast Elitist Multiobjective Genetic Algorithm NSGA-II. *Evol. Comput.* **2002**, *6*, 182–197.
31. Dalcali, A.; Akbaba, M. Comparison of 2D and 3D Magnetic field Analysis of Single-Phase Shaded Pole Induction Motors. *Eng. Sci. Technol. Int. J.* **2016**, *19*, 1–7. [CrossRef]

